JOURNAL OF CATALYSIS **63**, 35–52 (1980)

Concentration Profiles in Impregnation of Porous Catalysts: Nickel on Alumina

MASAHARU KOMIYAMA, ROBERT P. MERRILL, AND H. F. HARNSBERGER*

*School of Chemical Engineering, Cornell University, Ithaca, New York 14853, and *Chevron Research Company, Richmond, California 94802*

Received May 30, 1979; revised September 28, 1979

Impregnation procedures designed to control the radial concentration distribution of a supported metal catalyst were studied using $NiCl_2$ solutions and γ-alumina spheres. Equilibrium adsorption measurements for $NiCl_2$ on the alumina support showed a strong pH dependence and thus HNO_3 could be used to modify the adsorptivity of the γ-alumina for $NiCl_2$. Depending on the $NiCl_2$ and HNO_3 concentrations selected, a surface impregnation, a uniform impregnation, a subsurface impregnation, or the deposition of a subsurface band of nickel with the core of the sphere devoid of nickel resulted. A single-pore model was expanded to three dimensions assuming constant pressure differential throughout the support sphere. The model was consistent with actual impregnation profiles, both for one-component ($NiCl_2$) and two-component (HNO_3–$NiCl_2$) systems. Nickel concentrations were measured by light transmission through a thin section of the reduced catalyst and by an electron microprobe. Comparisons of the two measurements suggest that the size of the nickel crystallites deposited may depend on the pellet radius or that nickel aluminate may have formed during reduction in some cases. The drying step was found to cause segregation of $NiCl_2$ at the surface of the pellet in most cases, but such segregation could be suppressed by the use of a rapid drying program.

INTRODUCTION

Liquid-phase impregnation is a widely used technique for preparing a catalyst in which active catalytic crystallites are dispersed in a porous support with high surface area. The method involves (i) contacting a porous support with an impregnating solution which consists of a compound of a desired constituent dissolved in a liquid, (ii) drying the product, and (iii) calcining and reducing if necessary. Any of these steps can affect the particle size and final local concentration of the catalytic material upon the pore walls of the support.

It would be important in practical situations to predict and control the concentration profiles of the catalytic ingredients in supported catalysts. If, for example, the reaction is under the mass-transfer limiting conditions, it is desirable to have the catalytic constituent deposited near the external surface of the catalyst pellet, whereas a uniformly distributed profile is desired when the reaction is kinetically limited. If the reaction is poisoned by an impurity which is strongly adsorbed on the support, it may be best to produce a subsurface impregnation in which a band of catalyst-free support is established on the exterior of the pellet. The catalyst-free surface band can immobilize the poison, keeping it spatially separated from the active catalytic constituent. A subsurface impregnation may also be beneficial in service which produces catalyst attrition and loss of catalyst fines from the reactor space, because a catalyst with a subsurface impregnation will attrit only the support and retain the active metal.

Vincent and Merrill (*1*) have developed a model for the first step of the impregnation procedure, i.e., the time-dependent flow of impregnating solution into a dry pellet and interior dispersal of impregnant. Using a single-pore model, three parameters were found to play important roles in determining the concentration profile in this step: (i)

0021-9517/80/050035-18$02.00/0

the mass-transfer coefficient of the impregnant across the liquid–solid interface, or the adsorption rate, (ii) the equilibrium adsorption coefficient of the impregnant on the pore wall, and (iii) the relative capacity of the pore wall for adsorption (the ratio of the adsorption capacity of the wall to the adsorbate present in the filled pore at the initial concentration of the impregnating solution). The relative capacity and/or the adsorption coefficient are the easiest to adjust in practice by controlling the initial impregnant concentration and/or the impregnation temperature.

Chen and Anderson (*2*) impregnated γ-alumina spheres with chromic acid solutions of different concentrations. For a concentration of 0.4 *M* the central portion of the particle contained no chromium. Chromium was found in the central portion for higher concentrations of impregnating solutions used.

The impregnation profiles can also be controlled by altering the starting compound of the catalytic constituent. Roth and Reichard (*3*) prepared catalysts from platinum diaminodinitrite aqueous solution (catalyst A) or chloroplatinic acid aqueous solution (catalyst B). Catalyst A showed a nearly uniform platinum distribution, whereas in catalyst B, more platinum was deposited near the external surface than at the center of the pellet. The chemical species used in the impregnating solution, however, can have significant influence on the resulting metal particle size distribution (*4*) and/or other characteristics of the finished catalyst, and other means of controlling the radial concentration profile are often required.

Coimpregnation is yet another way to establish the desired concentration profiles. Maatman (*5*) has demonstrated that when alumina is impregnated with chloroplatinic acid, though there is a strong tendency toward external surface impregnation, uniform impregnation can be obtained by adding HCl, HNO_3, or various inorganic nitrates to the impregnating solution. Apparently the additives compete with the chloroplatinic acid for available adsorption sites and cause the surface adsorption capacity to saturate at much lower platinum levels, allowing the metal to penetrate deeper into the interior of the pellet.

It has been known that the adsorption of metal cations from aqueous solutions to various solid surfaces are strongly pH dependent (*4, 6, 7*). In general, the adsorption of metal cations increases dramatically above a certain pH. It is usually assumed that at a very low pH the metal cation to be adsorbed is in competition with the large excess of hydrogen ions. The increase in adsorption with pH has been attributed to the hydrolysis of either the solid surface or the metal ion (*6*). This pH dependence of the adsorptivity provides another degree of freedom in engineering the impregnation profiles.

The drying step of the impregnation method may also affect the profiles. Maatman and Prater (*8*) considered this process and speculated on the basis of an analysis of evaporation from a polydisperse pore structure that the catalytic ingredient would tend to redistribute into small pores and penetrate deeper into the interior of the pellet during the drying step. No experimental evidence, however, has been presented to support this prediction.

A general method for an accurate determination of radial metal concentration profiles in impregnated catalysts has been provided by the technique of electron microprobe analysis. Kempling and Anderson (9) determined the metal concentration profile in a commercial ruthenium–alumina catalyst, Roth and Reichard (*3*) examined the profiles in platinum–alumina catalysts, and Chen and Anderson (*2, 10*) studied the profiles in chromia–alumina catalysts. A summary of the use of electron microprobes in the study of catalysts is given by Purdy and Anderson (*11*).

Optical transmission analysis (measurement of turbidity) can also be used to measure these cncentration profiles. When light travels through a layer of scattering-absorbing particles, the incident light is partly scattered and partly absorbed by particles. According to the well-known Mie formula (*12*), the turbidity is directly proportional to the volume of the scattering-absorbing particles in the path, provided that the particle size is smaller than the incident light wavelength and no multiple scattering by the particles occurs (Rayleigh scattering). Hence if there is a difference between the refractive indices of the dispersed metal particles and catalyst support, it is possible to measure the impregnation profiles by choosing appropriate experimental conditions.

This paper reports an attempt to demonstrate how one might manipulate and control the impregnation profiles. Alumina pellets were impregnated with aqueous $NiCl_2$ solutions or coimpregnated with $NiCl_2$ and HNO_3. The nickel concentration profiles in the pellets were determined by two independent techniques: X-ray fluorescence in an electron microprobe, and optical transmission. When the results obtained by these techniques are compared, one can obtain some rudimentary information on the size of the metal crystallites within the support. The role of the drying step on the redistribution of catalytic ingredients was also studied. The one-dimensional single-pore model was extended to three dimensions, and the consistency of the model with the nickel-impregnated catalysts was examined.

EXPERIMENTAL

Spherical γ-alumina pellets of 4-mm diameter supplied by Universal Oil Products were employed as the porous support. To cull out spheres with macroscopic cracks and defects, the pellets were sorted by floating them in dibromomethane. Those with large macropores sunk while well-formed spheres continued to float. Pellets with visually obvious imperfections were also removed. The sorted pellets were dried at 110°C for 3 hr, calcined at 600°C in the air for 6 hr, and then stored under dry air at 130°C until used. The nitrogen adsorption isotherm at 77 K for the pretreated alumina gave a BET surface area of 132 m^2/g. The total pore volume measured by water displacement method was 1.67 cm^3/g (a pore volume fraction of 85%), and the average pore size was calculated to be 253 Å.

Aqueous-phase adsorption measurements, both kinetics and equilibrium, were carried out by soaking powdered precalcined alumina pellets (<65 mesh) in solutions of $NiCl_2$ or HNO_3 at 20°C. The amount of $NiCl_2$ adsorbed on the solid surface was determined spectrophotometrically from the incremental loss of Ni(II) species in the liquid phase, which was separated from the solid after a predetermined contact time by a centrifuge. HNO_3 adsorption was measured by monitoring the pH change in the solution. The rate of adsorption of $NiCl_2$ on alumina was very low after 10 hr of contact, and after 48 hr it achieved a quasi-equilibrium. The "equilibrium" adsorption isotherms were taken at 48 hr (2 days) and at 336 hr (2 weeks) of soaking. The adsorption of HNO_3 did not achieve even a quasi-equilibrium within 24 hr and no attempt was made to obtain the equilibrium data.

The pH dependence of the adsorption of $NiCl_2$ and $Ni(NO_3)_2$ on alumina powder was also measured after 1 hr contact time using HNO_3 or NH_4OH as pH modifier. One-hour contact times were used in an attempt to avoid alteration of the solid surface by the extended contact with acid or base and to simulate the catalyst impregnation time employed in the uptake experiments.

Nickel-on-γ-alumina catalysts were prepared by impregnating the pretreated alumina pellets with aqueous solutions of $NiCl_2$ or mixtures of $NiCl_2$ and HNO_3. During the impregnations the solutions were kept at 20.0°C and continuously stirred by a magnetic stirrer. The time required to fill the pellets completely with the solution was found to be 66 to 80 min depending on the concentration of the solutions, i.e., the solution's surface tension and viscosity (*13*) are affected somewhat by changes in the composition of the solution. Immediately after the pellets were filled with the impregnating solution they were removed and wiped. To examine the redistribution of the impregnant during the drying step, a portion of the pellets were sectioned through the center to form slabs of 1.2-mm thickness before they were dried.

The spherical pellets and slabs were dried and then reduced together in flowing hydrogen in a rotating furnace. The temperature program used during drying is summarized in Table 1. Most of the samples were processed under the standard conditions.

Optical transmission analysis of the catalysts was carried out by using an automatic recording microdensitometer manufactured by Joyce Loebel and Company Ltd. The reduced spherical pellets were sectioned to form slabs maintaining the symmetry with respect to the center of the pellets, and then the flat surfaces were polished by 600-grit abrasive paper to give a thickness of 150 μm for pellets of high nickel content and 1000 μm for ones of low nickel content. Such a procedure was necessary to maintain optical densities within the dynamic range of the instrument and to minimize multiple scattering. The slabs sectioned before the drying were also polished in the same manner. Polished samples were then immersed in α-bromonaphthalene, whose refractive index of 1.66 is nearly the same as that of γ-alumina which is 1.7. Thus the alumina substrate becomes nearly transparent, and the turbidity is only a function of the total volume of nickel particles within the light path. The specimen was placed in a glass sample holder as shown in Fig. 1. The vacancy in the holder was filled with α-bromonaphthalene to eliminate the refractive index discontinuity at the edge of the slab, which would have resulted in a spurious turbidity measurement. The sample magnification and the effective slit width were ×22 and 100 μm, respectively; hence the resolution was 4.5 μm.

TABLE 1

Temperature Program of the Drying and Reduction Step

Process	Temp. (°C)	Duration (hr)	Rate of Temp change (°C/hr)	
			Standard	Rapid drying
Heating	23–110	—	~100	~600
Drying	110	2	—	—
Heating	110–500	—	~500	~500
Reduction	500	12	—	—

The composition profiles of those samples which were used for the turbidity measurement were also analyzed with an ARL electron microprobe analyzer located at Chevron Research Laboratory, Richmond, California. The samples were imbedded in Bakelite and polished using SiC papers down to 3 μm diamond paste. Pearl oil was used in polishing, and hexane and toluene for rinse. The samples were then coated with a layer of evaporated carbon. Two standard samples with a known nickel content were also prepared by the same method and were used to calibrate the sensitivity of the analyzer for nickel. The sensitivily of the analyzer was assumed to be linear over the concentration range of interest. Point counting was performed along the diameter of the circular cross section at 25- to 40-μm intervals and with 10-μm beam spot size. The acceleration voltage of the electron beam was 20 kV, and the specimen current was 50 nA. Total nickel contents of each sample were also measured by standard chemical analysis.

MODELING

The one-dimensional single-pore model for concentration profiles in impregnation proposed by Vincent and Merrill (*1*) can be expanded to a three-dimensional spherical pellet.

The time-dependent flow of impregnating solution into a single pore and the deposition of impregnant upon the walls of the pores is expressed by the following simultaneous differential equations (*1*) for the case when mass transfer across the liquid–solid interface controls the overall rate of the impregnant removal:

$$\frac{\partial \psi}{\partial \tau} + u\frac{\partial \psi}{\partial \Gamma} = -K\left(\psi - \frac{\theta}{K_L(1-\theta)}\right), \qquad (1)$$

$$\frac{\partial \theta}{\partial \tau} = \frac{K}{\eta}\left(\psi - \frac{\theta}{K_L(1-\theta)}\right). \qquad (2)$$

If adsorption kinetics is rate controlling, the reduced mass-transfer coefficient, K, is replaced by a reduced adsorption coefficient, K_1. It should be recalled that the Langmuir equilibrium parameter, K_L, is simply K_1/K_2, where K_2 is a reduced desorption coefficient:

$$\frac{\partial \psi}{\partial \tau} + u\frac{\partial \psi}{\partial \Gamma} = -K_1\psi(1-\theta) + K_2\theta, \quad (3)$$

$$\frac{\partial \theta}{\partial \tau} = \frac{K_1}{\eta}\psi(1-\theta) - \frac{K_2}{\eta}\theta. \qquad (4)$$

The parameters used in Eqs. (1) through (4) are defined as follows:

$$\begin{aligned} \psi &= c/c_0, \\ \Gamma &= Z/L, \\ K &= 2k_m t_L/R \\ K_L &= K_L' c_0 \\ \eta &= 2c_s/Rc_0, \\ K_1 &= 2k_1 t_L/R, \\ K_2 &= 2k_2 t_L/Rc_0. \end{aligned} \qquad (5)$$

A list of symbols and their definitions appear in the Appendix. In the derivation of the equations plug flow has been assumed for the impregnating solution, and the axial dispersion of the impregnant along a length of a pore is assumed to be negligible. Moreover the equilibrium adsorption and the kinetics of adsorption and desorption of the impregnant at the pore wall were assumed to obey the Langmuir adsorption mechanism.

This single-pore model represented by Eqs. (1) through (4) can be expanded to a three-dimensional system by adopting an appropriate velocity, u. The single-pore model results in a velocity inversely proportional to the square root of time following the description of Washburn (*13*). Penetration rates in flat slabs should also follow the same velocity expression if the porous solid is approximated as a collection of pores of uniform radius.

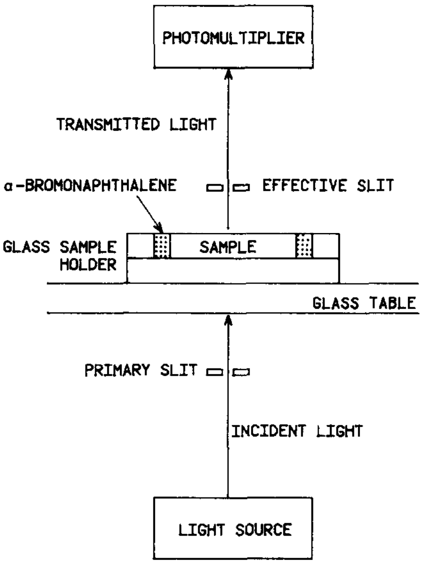

FIG. 1. Schematic diagram for the turbidity measurement.

Three-dimensional or spherical geometry, however, results in a velocity different from that used in the single-pore model. According to Washburn (*13*), the total volume, V, which penetrates in n cylindrical capillary tubes of a uniform radius, R, is

$$V = \frac{\pi}{2}At^{1/2}, \; A = \frac{1}{\mu^{1/2}}\sum^{n}(\Delta P^{1/2}R^3), \qquad (6)$$

where μ is the solution viscosity and ΔP is the pressure drop. The lumped constant A will be taken as independent of radius of the spherical pellet. This is equivalent to assuming a constant pressure drop throughout the pellet. The volume can also be expressed in terms of the radius of the pellet, L, and the position of the liquid front, $l(t)$, which is measured from the surface of the sphere:

$$V = \tfrac{4}{3}\pi k(L^3 - (L - l(t))^3). \qquad (7)$$

Differentiating both equations with respect to t and $l(t)$, respectively, and equating the resulting equations gives the radial velocity of the liquid front at $l(t)$:

$$u_l = \frac{dl}{dt} = \frac{A}{16k(L-l)^2 t^{1/2}}. \tag{8}$$

Because the volumetric flow rate at any radial position of the pellet, Z ($l \geqq Z \geqq 0$), is equal to that at $l(t)$, the velocity of the liquid at Z, u_Z, is related to u_l as

$$u_Z = u_l \frac{(L-l)^2}{(L-Z)^2}, \tag{9}$$

$$u_Z = \frac{A}{16k(L-Z)^2 t^{1/2}}. \tag{10}$$

Integrating Eq. (8) gives

$$(1-\Gamma)^3 = 1 - \tau^{1/2} \tag{11}$$

with $\tau = t/t_L$ and $t_L = [(8/3)(kL^3/A)]^2$.

Substitution of t_L into Eq. (10) gives

$$u_Z = \frac{L^3}{6 t_L^{1/2} (L-Z)^2 t^{1/2}}. \tag{12}$$

Finally, the nondimensionalized velocity, u, for spherical geometry is obtained:

$$u = \frac{u_Z t_L}{L} = \frac{1}{6(1-\Gamma)^2 \tau^{1/2}}. \tag{13}$$

Substituting Eq. (13) into Eqs. (1) and (3), one obtains

$$\frac{\partial\psi}{\partial\tau} + \frac{1}{6(1-\Gamma)^2\tau^{1/2}} \frac{\partial\psi}{\partial\Gamma} = -K\left(\psi - \frac{\theta}{K_L(1-\theta)}\right), \tag{14}$$

$$\frac{\partial\psi}{\partial\tau} + \frac{1}{6(1-\Gamma)^2\tau^{1/2}} \frac{\partial\psi}{\partial\Gamma} = -K_1\psi(1-\theta) + K_2\theta. \tag{15}$$

The simultaneous Eqs. (14) and (2) or (15) and (4) are easily solved numerically using a first-order finite difference technique.

An example for the adsorption kinetics limited case is computed and plotted in Fig. 2. Since the model assumes no axial diffusion along the radius of the pellet, it is so labeled. The fractional coverage of the pore wall, θ, when the impregnating solution reaches the center of the pellet ($\tau = 1$), is shown by the solid line. The impregnant in the liquid will eventually be adsorbed or redistributed on the pore wall during the subsequent drying step. One possibility is shown by the solid line, $\theta(\tau = \infty)$, assuming no axial diffusion or redistribution, i.e., the solute remaining in solution is eventually deposited "in place."

Assuming no axial diffusion obviously represents an extreme case and the other extreme can be visualized by assuming infinitely fast diffusion. In this case ψ continues to be unity at any τ and Γ, and hence Eqs. (14) and (15) vanish. θ in Eqs. (2) and (4) is then integrated as a function of either τ or Γ, which are related through the velocity u. For the adsorption kinetics limited case, the analytical expression for $\theta(\tau = 1)$ is

$$\theta(\tau = 1) = \frac{1}{1 + 1/K_L}\left(1 - \exp\left(-\frac{K_1}{\eta}(1 + 1/K_L)(1 - (1 - (1-\Gamma)^3)^2)\right)\right). \tag{16}$$

The computed result labeled "infinite-diffusion" is also shown in Fig. 2 along with the "zero-diffusion" case. $\theta(\tau = \infty)$ is obtained by superimposing $\theta(\tau = 1)$ and $\Gamma(\tau = 1)$, which is equivalent to assuming no axial diffusion or redistribution during the drying step.

When there is no saturation limit for adsorption, such as crystallite growth, or the existing saturation limit is never ap-

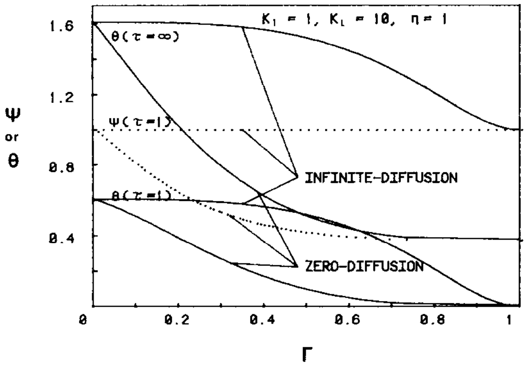

FIG. 2. Sample calculations of the three-dimensional model for zero-diffusion and infinite-diffusion schemes.

proached because c_0 is small, another limiting case, irreversible adsorption kinetics, arises (*1*). This results in small values of θ and thus Eq. (15) becomes

$$\frac{\partial\psi}{\partial\tau} + \frac{1}{6(1-\Gamma)^2\tau^{1/2}}\frac{\partial\psi}{\partial\Gamma} = -K_1\psi \quad (17)$$

and its analytical solution is given by

$$\psi = \exp(K_1(1-(1-\Gamma)^3)^2 - 2K_1\tau^{1/2}(1-(1-\Gamma)^3)). \quad (18)$$

The total impregnation at distance Γ is obtained by integrating the adsorption rates over time, using (18) for the concentration of liquid in contact with the surface after the liquid front has passed each radial position (*1*).

RESULTS

Figure 3 shows the kinetic adsorption measurements of $NiCl_2$ and HNO_3 from their aqueous solutions (blank squares for $NiCl_2$ and solid squares for HNO_3). The amount adsorbed is plotted as a function of time. The solid line is the Langmuir adsorption rate calculation for $NiCl_2$ using parameters obtained from 48-hr quasi-equilibrium data, and an adsorption rate coefficient k_1 chosen to give the best fit for the rate data. Neither the Langmuir rate equation nor a simple power law adsorption rate gave satisfying fits to the adsorption data for HNO_3.

Figure 4 shows the Langmuir plot of the isotherms of $NiCl_2$ at 48 hr, i.e., the quasi-equilibrium data (solid squares) and 336-hr (blank squares) of contact. The Langmuir adsorption coefficient, K_L', is the same for both the 48-hr and the 336-hr isotherms, but the adsorption capacity, c_s, is larger for the 336-hr data. The values of K_L, c_s, and the adsorption rate coefficient, k_1, are taken from the quasi-equilibrium data (48 hr) and shown in Table 2. Quasi-equilibrium data were used to obtain these parameters because the actual catalyst impregnation took only about 1 hr.

Figure 5 shows the pH dependence of $NiCl_2$ (blank square) and $Ni(NO_3)_2$ (solid square) adsorption after 1 hr soaking. Adsorption with no additives is shown by double squares. Both for higher pH (with NH_4OH) and for lower pH (with HNO_3), pH values of the solutions after adsorption were closer to those of pure nickel solutions than the starting pH values, indicating both HNO_3 and NH_4OH are adsorbed on γ-alumina along with nickel species. pH values plotted in the figure are those after adsorption.

Figure 6 shows nickel concentration and turbidity profiles of samples impregnated with solutions of several different $NiCl_2$ concentrations. The open squares are for samples not sectioned before drying; the solid squares for samples sectioned before drying and the dotted lines represent the concentration from turbidity measurements of samples not sectioned before drying;

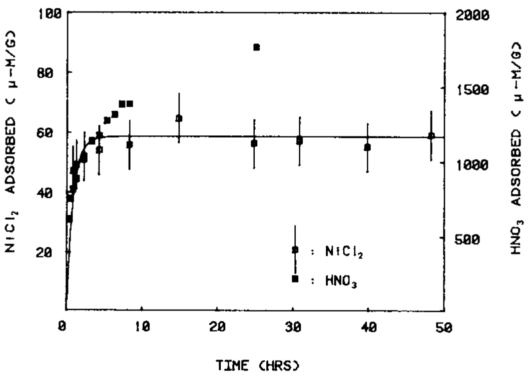

FIG. 3. Adsorption rate measurements of $NiCl_2$ and HNO_3 on γ-alumina.

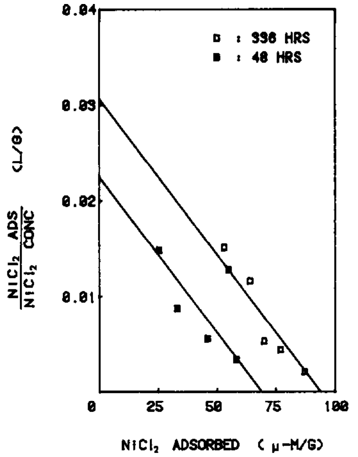

FIG. 4. Langmuir plots of $NiCl_2$ adsorption isotherms on γ-alumina.

and the solid lines are the model calculations. Sample 402 was impregnated with the same solution as sample 40 but was dried using the rapid drying program. Figure 7 shows the profiles of samples, coimpregnated with the impregnating solutions of a single HNO_3 level but different $NiCl_2$ concentrations. Figure 8 compares the profiles of samples impregnated with the solutions of a single $NiCl_2$ level but HNO_3 concentrations from 10^{-4} to 10^{-2} M.

The two standard samples used to calibrate the electron microprobe were a sample containing 6.1 wt% nickel and sample 60 (see Fig. 6), the nickel content of which was measured by chemical analysis. Sample 60 was chosen as a low concentration standard because it has a uniform nickel concentration profile, and thus the error introduced by integrating the microprobe profile is minimized. Comparison of total nickel content from chemical analysis, probe analysis, an expected amount from pore volume times impregnating solution concentration is given in Table 3.

TABLE 2

Adsorption Parameters of $NiCl_2$ and HNO_3 on γ-Alumina

	$NiCl_2$	HNO_3
Langmuir adsorption coefficient K'_L(liters/mole)	326	—
Adsorption capacity c_s(μmole/g)	68.9	—
Adsorption rate coefficient k_1(cm/sec)	8×10^{-10}	—
Initial rate coefficient (cm/sec)	—	1×10^{-9}

The turbidity is arbitrarily set to give the best general agreement with the impregnation profiles of all of the samples, including the coimpregnated catalysts. A turbidity of 100 cm^{-1} is consistent with 0.6 wt% nickel content. No probe analysis was done on sample 42 (Fig. 7), and its profile is shown only by optical transmission analysis.

For $NiCl_2$, the calculations were made only for the case of adsorption as the rate limiting deposition processes, but the results are not significantly different for the mass-transfer controlled deposition. For HNO_3 adsorption in Figs. 7 and 8, irreversible adsorption kinetics was applied because, for all the samples, c_0 of HNO_3 is very low compared with HNO_3 absorption capacity of alumina shown in Fig. 3. The adsorption times and adsorbate levels are more characteristic of the initial rates than those based on the Langmuir model. HNO_3 concentration profiles in the liquid phase are shown in the figures since the adsorptive inhibition correlates best with the final pH of the solution. The calculations of $NiCl_2$ profiles for these coimpregnated samples were done assuming that the adsorption of $NiCl_2$ is inhibited until HNO_3 in the penetrating solution is depleted to give the

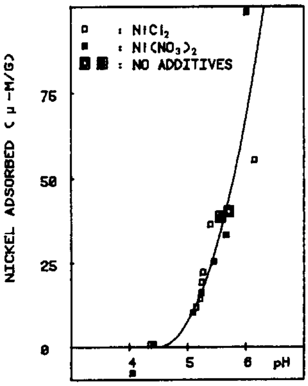

FIG. 5. pH effect on $NiCl_2$ and $Ni(NO_3)_2$ adsorption on γ-alumina.

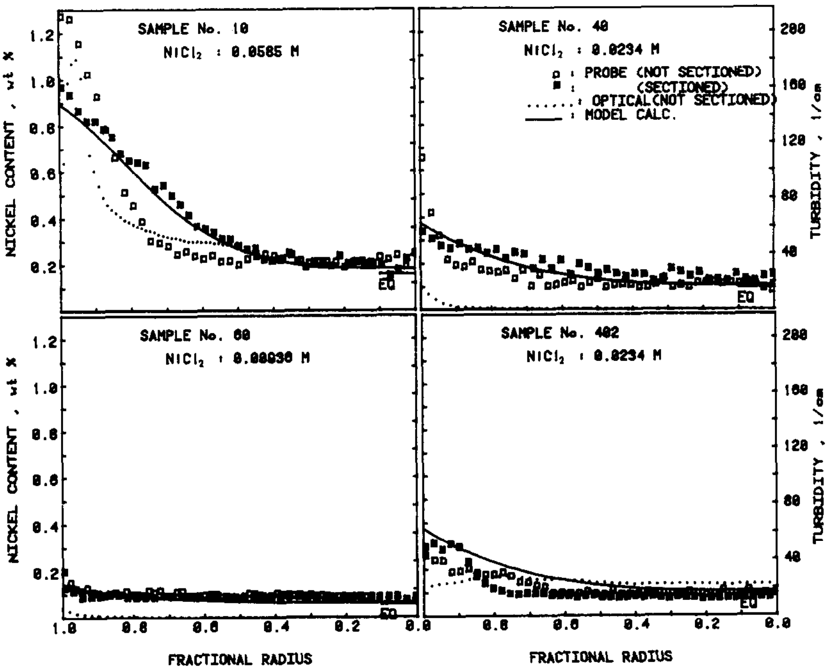

FIG. 6. Nickel concentration and turbidity profiles of samples impregnated with pure $NiCl_2$ solutions.

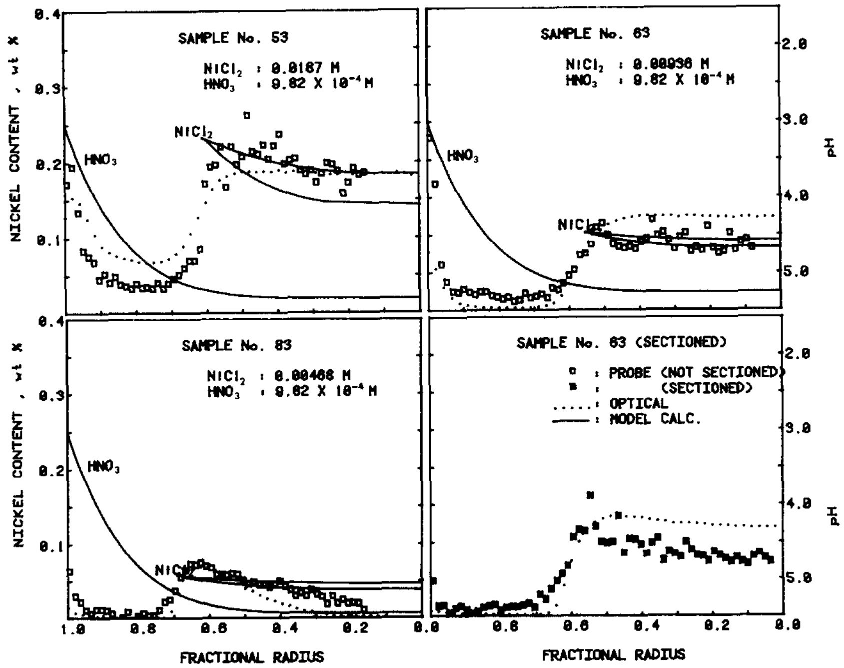

FIG. 7. Nickel concentration and turbidity profiles of coimpregnated samples, HNO_3 concentration profiles are for the liquid phase.

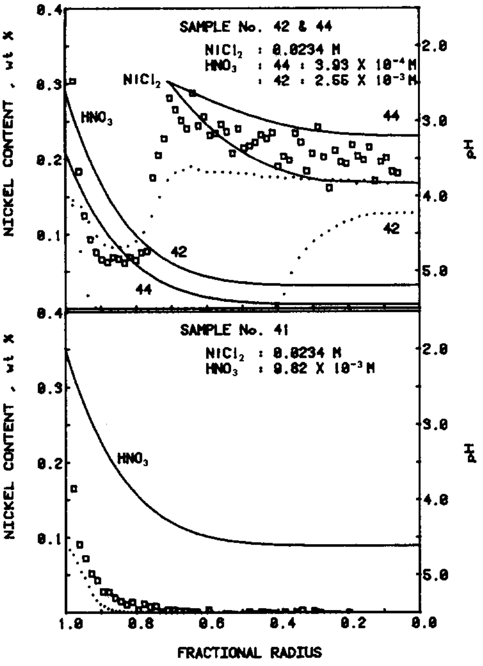

FIG. 8. Nickel concentration and turbidity profiles of coimpregnated samples, HNO_3 concentration profiles are for the liquid phase.

pH at which the adsorption inhibition decreases rapidly (pH ≈ 5.2; see Fig. 5). The breakthrough point was taken from the probe analysis. Because of the rather small volume fraction of the pellet available for $NiCl_2$ in these samples (for example, if the breakthrough occurs at $\Gamma = 0.4$, the uninhibited region occupies only 22% of the total volume), and because of the high $NiCl_2$ concentration up to the breakthrough point, it is expected that radial diffusion of $NiCl_2$ from the inhibited region could affect the profile significantly in the uninhibited region. Thus both the zero-diffusion (lower solid line) and infinite-diffusion (upper solid line) calculations are plotted. The actual profiles should fall in between these two lines. Other profiles are all based on the zero-diffusion scheme. For $NiCl_2$ the calculation is performed to the limit of $\tau = \infty$ assuming no axial dispersion after $\tau = 1$. For HNO_3 the calculation is terminated at $\tau = 1$. The adsorption or the axial diffusion (if any) during drying has little effect on the logarithmic pH; thus the breakthrough is altered only slightly.

The values of the parameters used for the model calculation are shown in Table 4. Among the parameters involved, the Langmuir equilibrium paramenter, K_L, and the relative capacity for adsorption, η, can be determined from the adsorption isotherm data, the physical properties of the alumina pellets, and the concentration of the impregnating solutions. The adsorption rate coefficient, k_1, is used as an adjustable parameter for the curve fitting the data.

DISCUSSION

Prediction and Control of One-Component Impregnation Profiles

As predicted by Vincent and Merrill in general (*1*), and as shown by Chen and Anderson for the chromia–alumina system (*2*), one-component impregnation profiles are easily controlled by changing the initial concentration of the impregnating solution, c_0. The nickel profiles shown in Fig. 6 demonstrate that this is also true for the nickel–alumina system. With the highest c_0, the profile has a high nickel content at the

TABLE 3

Comparison of Total Nickel Content from Microprobe Analysis, Chemical Analysis, and Expected Amount

Sample No.	Total nickel content (wt%)		
	Expected (pore vol × concn)	Chemical analysis	Probe analysis
10	0.547	0.725	0.609
40	0.229	0.278	0.205
402	0.229	—	0.159
60	0.092	0.088	0.091
41	0.229	0.078	0.046
42	0.229	—	—
44	0.229	0.380	0.172
53	0.183	0.243	0.098
63	0.092	0.090	0.055
83	0.046	0.033	0.029

TABLE 4

Values of the Parameters Used for the Model Calculations of Impregnation Profiles: Reversible ($NiCl_2$) and Irreversible Adsorption Kinetics

Sample No.	Impregnation time t_L (sec)	Relative capacity for adsorption $\eta = 2c_s/Rc_0$ ($NiCl_2$)	Langmuir equilibrium parameter $K_L = K'_L c_0$ ($NiCl_2$)	Reduced adsorption coefficient K_1		Adsorption coefficient $k_1 = RK_1/2t_L$ (cm/sec)	
				($NiCl_2$)	(HNO_3)	($NiCl_2$)	(HNO_3)
10	4800	0.705	19.07	1.2	—	3.2×10^{-10}	—
40	4500	1.76	7.63	0.8	—	2.2×10^{-10}	—
402	4500	1.76	7.63	0.8	—	2.2×10^{-10}	—
60	3960	4.41	3.05	0.4	—	1.3×10^{-10}	—
41	4200	1.76	7.63	—	6.0	—	1.8×10^{-9}
42	4200	1.76	7.63	—	6.0	—	1.8×10^{-9}
44	4200	1.76	7.63	0.6	4.7	1.8×10^{-10}	1.4×10^{-9}
53	4200	2.21	6.10	0.7	5.3	2.1×10^{-10}	1.6×10^{-9}
63	4200	4.41	3.05	0.4	5.2	1.2×10^{-10}	1.6×10^{-9}
83	4200	8.82	1.53	0.4	5.6	1.2×10^{-10}	1.7×10^{-9}

periphery, which gradually decreases toward the center of the pellet. As c_0 is decreased by half, the concentration near the external surface and the gradient into the interior are both lowered. When c_0 is further reduced, a uniform impregnation profile is produced.

On the basis of the three-dimensional model, the uniform impregnation profile is a characteristic of a system having low values of mass-transfer coefficient, K, and/or adsorption coefficient, K_1. With small K and/or K_1, the impregnating solution penetrates into the pellet without losing much of the impregnant onto the pore wall. As a result, all the interior surface of the pellet is exposed essentially to a uniform distribution of nickel throughout the pellet. The model calculation for the case of adsorption kinetics limiting the rate shows a very good agreement with the profile, and gives a value of the reduced adsorption coefficient, $K_1 = 0.4$, which is consistent with $k_1 = 1.3 \times 10^{-10}$ cm/sec. The value obtained for the powder experimentally is 8×10^{-10} cm/sec. When the mass-transfer limiting case is applied, the resulting fit is equivalent to that for the adsorption kinetics case, but the mass-transfer coefficient is unrealistically low.

As c_0 increases a catalyst starts to develop a profile with a higher nickel content near the exterior surface. This is due to the high driving force near the exterior where the penetrating solution still has high impregnant concentration, and is consistent with the low deposition rates, as shown in Table 4, where the rate coefficient deduced from the fits of the model calculation is essentially constant. The difference in profiles among the samples in Fig. 6 is, therefore, solely due to the difference in the initial concentration of the impregnating solutions, c_0, and hence the difference of the relative capacity for the adsorption, η, and the Langmuir adsorption parameter, K_L, which are both dependent on c_0.

To determine the rate-limiting step, the mass transfer coefficient, k_m, was estimated (*14*). Using the physical propoerties of pure water, physical dimension of the alumina pellets, and their average pore diameter, and 1×10^{-5} cm^2/sec as the molecular diffusion coefficient for $NiCl_2$, one obtains $k_m \cong 20$ cm/sec. This is orders of magnitude larger than that derived from curve fitting the data, $k_1 \cong 2 \times 10^{-10}$ cm/sec. Hence the process is obviously limited by adsorption kinetics and not by mass transport. This conclusion is supported by the fact that the k_1 value obtained from the adsorption rate measurement, 8×10^{-10} cm/sec is comparable to that obtained from the profile curve fitting.

The agreement shown between the three-dimensional model calculations and the experimental impregnation profiles indicates that reliable estimates of adsorption kinetics and equilibrium adsorption measurements may be sufficient to predict concentration profiles when adsorption kinetics limit the deposition rate.

pH-Controlled Subsurface Impregnation

As shown by the adsorption experiments on γ-alumina (Fig. 5), HNO_3 strongly inhibits nickel species from being adsorbed on the surface. Numerous studies on the pH effect on metal cation adsorption have been done on various metal–solid systems (*6*). In general, at low pH, adsorption of the metal cation is inhibited by the excess hydrogen ion which competes with the metal cation. Above a certain pH, either the metal cation or the solid surface is hydrolyzed and the adsorption of the metal cation or the hydrolyzed metal ion results.

If the pH-controlling species (HNO_3 in this case) is adsorbed on the pore wall, then as the solution penetrates the pore the pH continually increases. At some point along the axis of the pore the pH may increase to the point where adsorption of a coimpregnated metal cation becomes appreciable. This should result in an outer shell of metal-free adsorbate and a subsurface impregnation past the point where the critical pH is achieved, provided that molecular diffusion along the axis of the pore is small enough.

Every coimpregnation profile, shown in Figs. 7 and 8, can be divided into three regions: the first region is at the periphery, with high nickel content; the second is between the periphery and the core, with low or zero nickel content; and the third is the core, with high nickel content.

The high nickel content in the first region cannot be understood by pH-controlled coimpregnation. The adsorption sites at the periphery where pH is low should have been occupied only by HNO_3. The high nickel deposition found in the finished catalysts is, therefore, assumed to have occurred not during the impregnation but during the subsequent drying step. This suggests that the drying step causes the segregation of the impregnant left in the penetrated solution toward the exterior of the pellet and this phenomenon will be discussed later. In the first and the second regions, then, only HNO_3 is adsorbed during impregnation. HNO_3 concentrations in the liquid phase at $\tau = 1$ are calculated as a function of Γ by using the irreversible adsorption kinetics limiting case, and are plotted in Figs. 7 and 8 as pH.

When the penetrating solution is depleted of HNO_3 and the pH reaches the threshold, $NiCl_2$ starts to deposit. $NiCl_2$ impregnation profiles were calculated assuming no deposition until a certain point in the pellet and single-component behavior afterward. The points where deposition starts were determined from the actual profiles. In these samples, the actual profiles are expected to fall in between the zero- and infinite-diffusion profiles. The small volume fraction available for $NiCl_2$ adsorption and the high $NiCl_2$ concentration up to the breakthrough enhance the axial diffusion effect on the profiles. As Figs. 7 and 8 show, the nickel deposition lies well within that predicted by the two extremes of the model.

The adsorption rate constants, k_1, for HNO_3 as well as for $NiCl_2$, are essentially constant as shown in Table 4, indicating that the three-dimensional model is also applicable to pH-controlled coimpregnation.

It is not clear what the mechanism of the pH effect may be. It is known that the formation of mononuclear hydroxo complex (hydrolysis) of Al(III) and Ni(II) occurs at pH = 4 and 8, respectively (*15*), while the pH effect data (Fig. 5) show an abrupt adsorption increase at around pH 5.2. Tewari and Lee (*7*), who observed a marked increase of adsorption for Co(II) on various metal oxide surfaces between pH 6 and 8 although Co(II) hydrolysis occurs at around pH 8, suggest that the solid–liquid interface may have a higher pH than in the liquid bulk. This would result in metal ion hydrolysis at the solid surface at much lower bulk pH than expected. Hydrolysis of the solid surface, a change in the degree of hydration of either the metal ion or the solid surface, or an ion-exchange effect could be the cause of the pH effect.

The analysis of the total nickel content in Table 3 shows that the microprobe underestimates samples except sample 60, which was used as the lower-range calibration standard. The microprobe scans always started one step inside from the sample edge. The volume fraction of one step at the edge is as high as 10% of the the total volume and for the samples which have sharp nickel concentration peaks at the edge, the error introduced by neglecting the first step could be large and it is likely that this is the source of the discrepency.

Chemical analysis of some of the samples shows more nickel than expected from the product of pore volumes and the solution concentration. This enhanced uptake is due to the molecular diffusion of the solute outside of the pellet into the interior during the 1-hr impregnation. The amount is not so large that the diffusion term in the impregnation model (*1*) has to be retained. Sample 41 (see Fig. 8), which is impregnated with the highest HNO_3 concentration, shows much less nickel than expected. This could be explained by the partial exclusion of solute ions from pores (*8*, *16*).

Three possible mechanisms for the partial exclusion phenomena have been proposed (*17*): (i) a change in the molecular volume of the adsorbed phase compared to that in the bulk liquid; (ii) exclusion of a species from pores whose radius is too small; and (iii) a "geometric effect" in which the center of a large species cannot approach the surface as closely as the center of a small species. In the time-dependent flow of liquid from the exterior to the interior of these pellets, however, the uptake times are short compared to the time required to relax axial diffusion gradients. The liquid in the interior of the pellet is not expected to be in equilibrium with the solution outside of the pellet, and the contribution of the first and the third mechanisms to the partial exclusion should be small. High concentrations of HNO_3 may exclude solute in either of two ways. Structure may be induced around the nickel cation increasing its size, or the double layer near the pore wall may be increased, thereby decreasing the effective pore radius.

The adsorption measurements for the powder (Fig. 5) also show the partial exclusion phenomenon. The run which ended with a final pH of 4.0 had a higher nickel concentration in the solution than when it was started. This is shown as a negative adsorption in Fig. 5. Assuming no nickel adsorption, it is calculated that the equivalent of 50% of the pore volume was not available to the nickel ion.

Surface Segregation during Drying

Sample 63, in Fig. 7, shows how the impregnant can be redistributed during the drying step. When the impregnation step has just finished, no $NiCl_2$ has been deposited on the pore wall in the neighborhood of the exterior of the pellet due to the low pH near the exterior. All of the $NiCl_2$ is expected to remain in the solution. Comparing the open squares (unsectioned before drying) with the filled squares (sectioned before drying) demonstrates that the drying results in an additional deposition at the exterior of the pellet (surface segregation).

This surface segregation is also demonstrated in sample 41 (Fig. 8), which has the highest HNO_3 concentration of all the work reported. It is so high in fact that the critical pH(5,2) for the $NiCl_2$ adsorption is never achieved within the pellet. Thus during impregnation, no nickel is deposited and all of the fluid within the pores before drying has a uniform nickel concentration. The shape of the entire concentration profile, which increases monotonically toward the exterior of the pellet, results from surface segregation during the drying step.

The result of comparing pellets sectioned before drying with those sectioned after drying is shown schematically in Fig. 9. In a spherical pellet drying occurs isotropically, whereas in a sectioned pellet it proceeds normal to the flat surfaces. Therefore, if accumulation of impregnant occurs at the surface where the drying takes place, the spherical pellet will have a wider band of redistributed impregnant at its exterior surface. In the sectioned pellet, this band is at the flat surfaces, which are polished off before measurements of the nickel content with the microprobe take place. Hence, the effect of the redistribution should be largely eliminated in the sectioned pellets.

Most of the sectioned pellets experienced a decrease in nickel content at their periphery without altering the other parts of their profiles appreciably. The drying step is thus shown to be the cause of segregation of impregnant near the exterior of the pellet. Evidence of surface segregation is also present in the profiles for pure nickel solutions shown in Fig. 6.

Not all of the solute left in the penetrating solution at the end of impregnation is segregated to the external surface. Drying requires a finite time and some axial diffusion and/or desorption with subsequent readsorption elsewhere while the wet pellet is warm is possible. The good agreement between the model calculation, which assumed no diffusion along the pore, and the actual profiles for single-component impregnation, suggests that solutes are adosrbed strongly on the pore wall even at drying temperatures. In fact, it is shown by the model calculation that the nickel content at the center of these samples is close to the expected equilibrium between the penetrated solution and the pore wall, which is shown in Fig. 6 by short lines labeled "EQ" at the right of each profile. Thus the amount of solute to be segregated by drying is expected to be relatively small, and the differences between sectioned and unsectioned pellets in Fig. 6 is correspondingly small. The amount segregated decreases as c_0 decreases, to the point that it is undetectable in sample 60. This is not true for the coimpregnated samples where the inhibited region does not adsorb any solute and the solute within the inhibited region is all subject to the segregation during drying. Thus the surface segregation shown for sample 63 in Fig. 7 is quite dramatic in comparison to the uninhibited samples.

The model calculation for sample 10 in

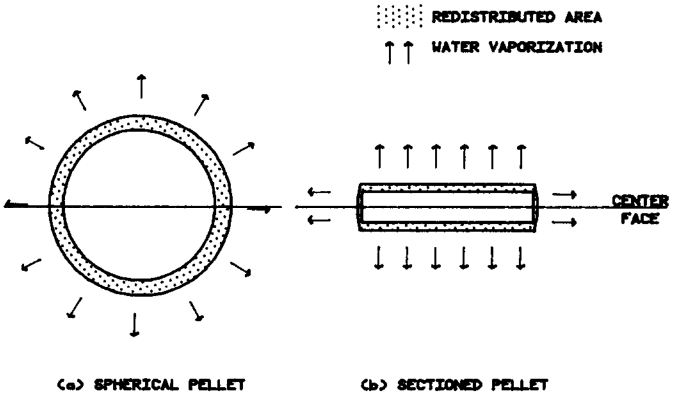

(a) SPHERICAL PELLET (b) SECTIONED PELLET

FIG. 9. Surface segregation of impregnant during the drying step.

Fig. 6 agrees better with the sectioned profile. For the sectioned pellet, the center face where the profile was measured is the very last plane to be dried and is most unaffected by the redistribution. The comparison of the sectioned and the unsectioned sample 10 shows that the redistribution mainly occurs from the subsurface band (fractional radius of 0.9 ~ 0.5) to the surface band (1.0 ~ 0.9), and the core (0.5 ~ 0) does not contribute to the segregation. The same is observed in sample 40, although the profile difference at the midsection is not so clear as that of sample 10. In sample 60, again due to the low c_0, the difference is undetectable.

Sample 402 in Fig. 6, by comparison with sample 40, does not show any appreciable surface segregation, and the sectioned pellet has a profile identical to that of the unsectioned one. Sample 402 is identical with sample 40 except for the drying step. Sample 402 was dried with the rapid drying program, a heating rate of 600°C/hr, compared to 100°C/hr for sample 40. The fact that sample 402 does not show any surface segregation indicates that the redistribution is dependent on the drying rate.

A possible mechanism for the drying and the surface segregation is as follows. Consider first a pellet consisting of uniform pores. When the pellet filled with impregnating solution is subjected to heating, heat is transferred from the external surface to the interior of the pellet, establishing a temperature gradient. Evaporation of water begins at the external surface, resulting in a receding gas–liquid interface. The impregnant in the solution increases its concentration at the menisci and it begins to deposit on the pore wall when the concentration exceeds the saturation point or, if the drying proceeds slowly enough, it diffuses into the remaining liquid. As a result, pellets with uniform pores have a tendency to redistribute the impregnant toward the center of the pellet.

For a pellet consisting of macro- and micropores, the situation is more complicated. Consider a macropore with branches of micropores as shown in Fig. 10. Water vaporization starts from the macropore because of the higher vapor pressure in macropores than the micropores. As vaporization in the macropores occurs, the interface recedes and the external surface of the pellet reaches a temperature high enough for liquid in micropores to evaporate. The liquid interface within the micropores will not recede, however, as long as they are in contact with larger pores. Instead they tend to draw liquid from the macropores because of their higher capillary pressure. Hence, the liquid lost by vaporization in the micropores is supplied from the macropore, which works as a "reservoir" of solution. Nearly all of the vaporization takes place close to the external surface and thus most of the solute is deposited there.

When the heating rate is slow enough and macro- and micropores are highly interconnected to allow micropores near the external surface to reach reserviors deep in the pellet, it is likely that a steady-state position is established very near the external surface and does not move into the interior of the pellet until most of the evaporation and hence most of the accumulation of the impregnant is completed. Gas-phase nitrogen adsorption measurements showed that the alumina pellets used for this study consist of a wide range of macro- and micropores. Apparently under the standard drying condition, which involves a low heating rate of 100°C/hr, the redistribution of the impregnant occurred mostly at or near the external surface of the pellets, but the

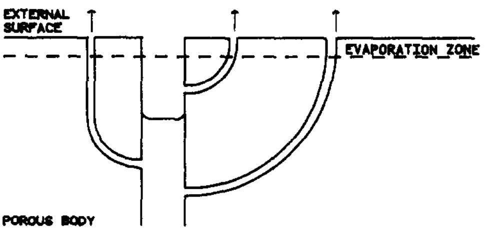

FIG. 10. Possible drying mechanism responsible for surface segregation.

600°C/hr is rapid enough to force the evaporation zone to move continuously toward the center of the pellet, and hence the redistribution occurs uniformly throughout the pellet.

Turbidity and Metal Crystallite Size

When the size of scattering-absorbing particle is smaller than the incident light wavelength, λ, and no multiple scattering by the particles occurs (Raleigh scattering), the turbidity, γ, is related to the sample thickness, x, and the ratio of intensities of incident and transmitted light:

$$I/I_0 = \exp(-\gamma x). \tag{19}$$

The turbidity is then a function of number density of particles, N, their complex index of refraction, m, and their volume, v, through the Mie formula (*10*)

$$\gamma = CNv, \tag{20}$$

where

$$C = -\frac{6\pi}{\lambda} \operatorname{Im}\left[\frac{m^2 - 1}{m^2 + 2}\right]. \tag{21}$$

When the scattering-absorbing particles are surrounded by a medium, m is a refractive index difference between the particles and the medium. Thus, γ is proportional to the total volume of scattering-absorbing particles in the light path.

The constant C can be determined experimentally for a system of monodisperse particles suspended in the same medium with a known number density. In the present study the turbidity is arbitrarily set to give the best agreement with microprobe measurements of the impregnant profiles for all of the samples. This gave C a numerical value of 167 cm^{-1} (Ni wt%)$^{-1}$.

The Mie formula assumes no multiple scattering of the incident light. This criterion is satisfied if the optical density is less than 0.3 (*12*). In the present experiment, the optical density was allowed to go up to 2, and, as most of the coimpregnated samples show, the linearity between γ and Nv holds quite well even above the Mie formula's criterion. It is possible, for example, that empirical determination of C over the range of optical densities employed is sufficient to compensate for small multiple scattering contributions. Nevertheless, minor discrepancies between the turbidity and microporbe profiles are to be expected.

In the region where the quasi-linearity between turbidity and nickel content holds, there are two samples which show a prominent discrepancy between the turbidity and the microprobe profiles: samples 40 and 60 in Fig. 6. The discrepancy suggests a drastic change in the particles' refractive index, m, which alters the value of C. Since dielectric properties are a strong function of the chemical state of matter, it is not surprising that dispersed nickel particles may have a different refractive index depending on how strongly they interact with the support. The interaction could be influenced by the degree of dispersion of the nickel particles: the smaller crystallites may have the stronger interaction with the substrate. The sudden turbidity change between sample 10 and samples 40 and 60 may indicate a much smaller average crystallite size for samples 40 and 60.

The refractive index is also altered by the formation of a new chemical species. According to Morikawa and his co-workers (*18*), who made a systematic study of the correlation between the method of preparation of a nickel–alumina catalyst and their physical and chemical properties, a considerable amount of nickel aluminate is found to be formed during the preparation of the catalyst in many cases. They report nickel aluminate formation at calcination temperatures as low as 300°C (*19*). It should be noted that sample 402, which differs from sample 40 only by the drying rate, does not exhibit this anomaly. More detailed consideration of this point will require additional experiments directed toward measuring crystallite size and the identification of chemical state, both as a function of pellet radius.

CONCLUSIONS

Radial concentration profiles in catalysts formed by impregnating γ-alumina spheres with aqueous nickel solutions have been determined. The profiles showed a strong dependence on the initial $NiCl_2$ concentration. Utilizing the pH effect on adsorption, subsurface impregnation was achieved by coimpregnating alumina pellets with $NiCl_2$ and HNO_3. HNO_3 concentration controlled the width of the catalyst-free surface band while $NiCl_2$ concentration controlled the profile and loading at the core. A three-dimensional impregnation profile model developed was consistent with actual profiles and with equilibrium and kinetic adsorption data. The drying step was found to cause surface segregation of the impregnant but increasing the drying rate suppressed the segregation. Comparison of profiles obtained by electron microprobe and optical transmission suggested the possibility of nickel aluminate formation or a drastic change in nickel particle size for some of the samples.

APPENDIX: SYMBOLS

A	lumped constant that involves multipore pressure drop [Eq. (6)]
C	scattering cross section [Eq. (21)]
c	concentration, moles/cm^3
c_s	adsorption capacity per unit area of pore wall, moles/cm^2
c_0	external concentration
I	transmitted light intensity
I_0	incident light intensity
k	porosity
k_m	mass transfer coefficient, cm/sec
k_1	adsorption rate coefficient, cm/sec
k_2	desorption rate coefficient, moles/cm^2 sec
K	reduced mass transfer coefficient, $2k_m t_L/R$
K_1	reduced adsorption coefficient, $2k_1 t_L/R$
K_2	reduced desorption coefficient, $2k_2 t_L/Rc_0$
K_L	Langmuir equilibrium parameter, $K'_L c_0$
K'_L	Langmuir adsorption coefficient, cm^3/mole
$l(t)$	instantaneous penetration of liquid in pore or radial position of penetration in sphere, measured from the surface, cm
L	pore length or radius of spherical pellet, cm
m	refractive index of dispersed nickel particles
N	number density of dispersed nickel particles
ΔP	pressure drop, dyn/cm^2
R	pore radius, cm
t	time, sec
t_L	time to fill pellet completely with liquid, sec
u	reduced velocity, $u_Z t_L/L$
u_l	liquid front velocity, cm/sec
u_Z	flow velocity at radical position Z cm/sec
V	volume of penetration, cm^3
v	volume of a dispersed nickel particle
x	sample thickness
Z	radial position in sphere, measured from the surface, cm
Γ	reduced radial position in sphere, Z/L, $1 -$ (fractional radius)
γ	turbidity [Eq. (19)]
μ	solution viscosity, P
λ	wavelength of light
τ	reduced time, t/t_L
ψ	reduced concentration, c/c_0
θ	fractional coverage of adsorption sites
η	relative capacity for adsorption, $2c_s/Rc_0$

ACKNOWLEDGMENTS

The work was partially supported by AFOSR Contract F 49620-77-C-0118. The γ-alumina pellets were supplied by Universal Oil Products Company. Part of the experimental work was done at the University of California, Berkeley. The microprobe measurements were done at Chevron Research Company, Richmond, California.

REFERENCES

1. Vincent, R. C., and Merrill, R. P., *J. Catal.* **35,** 206 (1974).
2. Chen, H. C., and Anderson, R. B., *Ind. Eng. Chem. Prod. Res. Develop.* **12,** 122 (1973).
3. Roth, J. F., and Reichard, T. E., *J. Res. Inst. Catal. Hokkaido Univ.* **20,** 84 (1972).
4. Bensi, H. A., Curtis, R. M., and Studer, H. P., *J. Catal.* **10,** 328 (1968).
5. Maatman, R. W., *Ind. Eng. Chem.* **51,** 913 (1959).
6. For example, Stryker, L. J., and Matijević, E., *In* "Adsorption from Aqueous Solution" (W. J. Weber and E. Matijević, Eds.), Advances n Chemistry Series 79, p. 62. Amer. Chem. Soc., Washington, D. C., 1968.
7. Tewari, P. M., and Lee, W., *J. Colloid Interface Sci.* **52,** 77 (1975).
8. Maatman, R. W., and Prater, C. D., *Ind. Eng. Chem.* **49,** 253 (1957).
9. Kempling, J. C., and Anderson, R. B., *Ind. Eng. Chem. Process Des. Develop.* **9,** 116 (1970).
10. Chen, H. C., and Anderson, R. B., *J. Catal.* **43,** 200 (1976).
11. Purdy, G. R., and Anderson, R. B., *in* "Experimental Methods in Catalytic Research" (R. B. Anderson, P. T. Dawson, Eds.), Vol. 2, Chap. 3. Academic Press, New York, 1976.
12. van de Hulst, H. C., "Light Scattering by Small Particles." Wiley, London, 1957.
13. Washburn, F. W., *Phys. Rev.* **17,** 273 (1921).
14. Bird, R. B., Stewart, W. E., and Lightfoot, E. N., "Transport Phenomena," p. 642. Wiley, New York, 1960.
15. Ringbom, A., "Complexation in Analytical Chemistry," p. 45, Inter Science, New York, 1963.
16. Dalton, R. W., McLanahan, J. L., and Maatman, R. W., *J. Colloid Sci.* **17,** 207 (1962).
17. Maatman, R., Poel, M., and Mahaffy, P., *J. Colloid Interface Sci.* **48,** 134 (1974).
18. Morikawa, K., Shirasaki, T., and Okada, M., *in* "Advances in Catalysis" (D. D. Eley, H. Pines, and P. B. Weisz, Eds.), Vol. 20, p. 87. Academic Press, New York, 1969.
19. Morikawa, K., and Nozaki, F., *Kogyo Kagaku Zasshi* [J. Ind. Chem. Japan] **64,** 54 (1961).